



# Hole storage overlayer of amorphous hafnium oxide for boosting hematite-based solar water splitting



Weicong Li<sup>a</sup>, Hongying Guo<sup>a</sup>, Chenyang Xu<sup>a</sup>, Chenke Tang<sup>a</sup>, Jae Sung Lee<sup>c,\*</sup>,  
Hemin Zhang<sup>a,b,\*\*</sup>

<sup>a</sup> College of Materials Science and Engineering, Sichuan University, Chengdu 610065, China

<sup>b</sup> Engineering Research Center of Alternative Energy Materials and Devices, Ministry of Education, Chengdu 610065, China

<sup>c</sup> School of Energy and Chemical Engineering, Ulsan National Institute of Science and Technology (UNIST), 50 UNIST-gil, Ulsan 44919, Republic of Korea

## ARTICLE INFO

### Keywords:

Hybrid microwave annealing  
Hematite photoanodes  
Hafnium engineering  
Hole storage layer  
Photoelectrochemical water splitting

## ABSTRACT

Hole storage layer (HSL) has been proved to be effective for constructing highly efficient photoelectrochemical (PEC) systems owing to its timely extraction and temporary storage of the photogenerated holes. Here we demonstrate an ultrathin HSL of amorphous hafnium oxide ( $\text{HfO}_x$ ) by a combined strategy of hybrid microwave annealing (HMA) and in-situ Hf doping, which enhances the PEC performance collaboratively: i) in-situ doping of  $\text{Hf}^{4+}$  ions into hematite lattices to enhance the electrical conductivity in the bulk; and ii) amorphous  $\text{HfO}_x$  overlayer on hematite surface as a HSL to promote efficient charge separation between electrons and oxidizing equivalents in water oxidation. As a result, the fabricated  $\text{Hf:Fe}_2\text{O}_3$  @ $\text{HfO}_x$  nanorod photoanode achieves a photocurrent density of  $3.47 \text{ mA cm}^{-2}$  at  $1.23 \text{ V}_{\text{RHE}}$  under simulated sunlight ( $100 \text{ mW cm}^{-2}$ ). With  $\text{NiCoFe}(\text{OH})_x$  co-catalyst modification, the photocurrent density further increases to  $4.13 \text{ mA cm}^{-2}$  at  $1.23 \text{ V}_{\text{RHE}}$ , which is 3 times higher than that of bare hematite ( $1.24 \text{ mA cm}^{-2}$ ) and comparable to the state-of-the-art hematite photoanode performance. This work demonstrates the high potential of the HMA-induced engineering of transition metal oxides applicable to the field of solar energy conversion.

## 1. Introduction

High solar-to-hydrogen (STH) conversion efficiency has been pursued persistently since the photoelectrochemical (PEC) water splitting into  $\text{H}_2$  and  $\text{O}_2$  was demonstrated with a  $\text{TiO}_2$  photoelectrode in 1972 [1, 2]. Owing to earth abundance and intrinsic stability in aqueous solution, metal oxide semiconductors have been extensively studied as potential photoelectrode materials, such as  $\text{WO}_3$ ,  $\text{BiVO}_4$ ,  $\text{Fe}_2\text{O}_3$ ,  $\text{FeTi}_2\text{O}_5$  and  $\text{Cu}_2\text{O}$  [3–7]. Among them, hematite ( $\alpha\text{-Fe}_2\text{O}_3$ ) is considered an ideal candidate material because of its suitable band gap ( $\sim 2.1 \text{ eV}$ ), non-toxicity, low cost, and good stability in alkaline solution [8,9]. However, hematite also suffers from a large onset potential ( $V_{\text{on}}$ ), poor charge mobility ( $0.01\text{--}0.1 \text{ cm}^2 \text{ S}^{-1} \text{ V}^{-1}$ ) [10], short hole diffusion distance (2–4 nm), and sluggish oxygen evolution reaction (OER) kinetics [11–13]. For these reasons, the achieved state-of-the-art STH conversion efficiency is still far below its theoretical value ( $\sim 15.5 \%$ ) [14,15].

Generally, the PEC performance of hematite is severely limited by

the low separation efficiency of photogenerated electron-hole pairs at bulk as well as surface. The low intrinsic conductivity of hematite reduces the lifetime and diffusion length of charge carriers, which decreases the charge separation efficiency in the bulk. Furthermore, slow kinetics of water oxidation reaction influences the charge separation efficiency on the surface of the photoanode. In order to meet these challenges, various elaborate modification strategies have been implemented at different parts of the hematite photoanodes. Doping different high-valence ions ( $\text{Sn}^{4+}$ ,  $\text{Ti}^{4+}$ ,  $\text{Nb}^{5+}$ ,  $\text{Ta}^{5+}$ ,  $\text{Ge}^{4+}$ ) can increase the concentration and lifetime of charge carriers to improve electric conductivity in the bulk. This is an effective way to promote PEC performance, but it also has negative side effects by introducing defects and structural disorders [9,15–18]. Dhandole et al. reported that fluorine, zirconium co-doped hematite showed an improved PEC performance by promoting photogenerated electron transport in the bulk [19]. In particular, a surface hole-storage layer (HSL) has been proved to be an effective approach to promote hole extraction/separation, which increases the

\* Corresponding author.

\*\* Corresponding author at: College of Materials Science and Engineering, Sichuan University, Chengdu 610065, China.

E-mail addresses: [jlee1234@unist.ac.kr](mailto:jlee1234@unist.ac.kr) (J.S. Lee), [hmzhang@scu.edu.cn](mailto:hmzhang@scu.edu.cn) (H. Zhang).

hole diffusion length to the surface and improves the separation efficiency of charge carriers [20–25]. Liu et al. demonstrated that a  $\text{Ni}(\text{OH})_x$  hole-storage layer between  $\text{Ta}_3\text{N}_5$  and coupled molecular catalysts restrained the charge recombination, leading to a photocurrent density ( $J_{\text{ph}}$ ) of  $12.1 \text{ mA cm}^{-2}$  at  $1.23 \text{ V}_{\text{RHE}}$  (close to the theoretical value of  $\text{Ta}_3\text{N}_5$ ) [20].

Recently, hybrid microwave annealing (HMA) has been demonstrated to be a good alternative to conventional thermal annealing (CTA) in fabrication of highly efficient photoelectrodes by completing very high-temperature reactions in an extremely short time (a few minutes) [26], thus offering many distinctive advantages over CTA, such as maintaining the original morphology of nanostructures, making less damage to FTO, and inducing unconventional high-temperature reactions [7,27,28]. It should be noted that a reductive atmosphere is produced around the sample during the HMA process since graphite powder is used as a susceptor, which leads to the production of  $\text{CO}$  and  $\text{CO}_2$  by partial combustion of the graphite. On the other hand, hafnium (Hf) has not been studied much as a dopant for hematite. A low concentration of Hf doping into hematite was proposed to be beneficial for formation of additional free electron polarons in the band structure according to a density functional theory (DFT) calculation [29]. Moreover, Hf doping from the surface could effectively reduce the diameter of hematite nanorods to increase the active surface area [30].

Here we report for the first time that hafnium engineering ameliorates hematite photoanodes in the bulk and surface. In detail, in-situ doping of  $\text{Hf}^{4+}$  ions into hematite lattices enhances the electrical conductivity in the bulk. Unexpectedly, the formation of an amorphous  $\text{HfO}_x$  layer on the hematite surface was found to become a HSL, which promoted surface charge separation effectively. This hole storage effect by an amorphous  $\text{HfO}_x$  layer for extracting/collecting photogenerated holes from hematite has never been reported before. Thus, the finally-engineered  $\text{Hf:Fe}_2\text{O}_3 @\text{HfO}_x$  photoanode exhibited a photocurrent density ( $J_{\text{ph}}$ ) of  $3.47 \text{ mA cm}^{-2}$  at  $1.23 \text{ V}_{\text{RHE}}$  under standard 1 sun condition. Additional  $\text{NiCoFe(OH)}_x$  co-catalyst modification further enhanced  $J_{\text{ph}}$  to  $4.13 \text{ mA cm}^{-2}$  at  $1.23 \text{ V}_{\text{RHE}}$ , which is 3 times higher than that of bare hematite ( $1.24 \text{ mA cm}^{-2}$ ).

## 2. Experimental methods

### 2.1. Fabrication of $\text{Hf:FeOOH}@\text{HfOCl}_2$ on FTO

Several pieces of F-doped tin oxide glass (FTO, TEC8,  $6\text{--}9 \Omega$ , Pilkington) were ultrasonically cleaned by deionized water, ethanol, and acetone in sequence, which makes FTO surface sufficiently hydrophilic. Then, the FTO was immersed into a 25 mL aqueous solution of 1.0 g  $\text{FeCl}_3 \cdot 6 \text{ H}_2\text{O}$  (Aladdin, 99.0 %), 2.1 g  $\text{NaNO}_3$  (Aladdin, 99.0 %), 100  $\mu\text{l}$   $\text{HNO}_3$  (Aladdin, 35.0 %), and an appropriate amount of  $\text{HfCl}_4$  solution, and kept in an electric oven at  $100^\circ\text{C}$  for 2–3 h two times to obtain a yellow thin film of  $\text{Hf:FeOOH}$  nanorods on the FTO substrate. After completely rinsing by deionized water, the obtained  $\text{Hf:FeOOH}$  was spin-coated with different concentrations of  $\text{HfCl}_4$  solutions to obtain  $\text{Hf:FeOOH}@\text{HfOCl}_2$ .

### 2.2. HMA-synthesized core-shell structure of $\text{Hf:Fe}_2\text{O}_3 @\text{HfO}_x$ photoanodes

Graphite powder (60 ~ 80 mL) was put in a Pyrex beaker (100 mL), which serves as a susceptor. The prepared sample was put on the slightly compacted graphite powder and treated in a home-made microwave oven (2.45 GHz, 1000 W) for 2–3 min at full power (100 %) to convert yellow  $\text{Hf:FeOOH}@\text{HfOCl}_2$  to red  $\text{Hf:Fe}_2\text{O}_3 @\text{HfO}_x$  photoanode.

### 2.3. Cocatalyst loading

For depositing  $\text{NiCoFe(OH)}_x$  as an OER catalyst on  $\text{Hf:Fe}_2\text{O}_3 @\text{HfO}_x$ , the fabricated photoanodes were immersed into a  $\text{NiCoFe(OH)}_x$

precursor solution for 25 min at room temperature, which was prepared with 10 mM  $\text{FeCl}_3 \cdot 6 \text{ H}_2\text{O}$ ,  $\text{NiCl}_2 \cdot 6 \text{ H}_2\text{O}$  (Aladdin, 99.0 %), and  $\text{CoCl}_2 \cdot 6 \text{ H}_2\text{O}$  (Aladdin, 99.0 %).

### 2.4. Physical characterization

X-ray photoelectron spectroscope (XPS) was performed on a Thermo Scientific spectrometer (K-Alpha) with  $\text{Al K}_\alpha$  radiation ( $h\nu = 1486.6 \text{ eV}$ ). High-angle annular dark-field scanning transmission electron microscopy (HAADF-STEM) images, corresponding electron energy loss spectroscopy (EELS) mapping and linear scan were carried out on a Titan Themis Z machine (Thermo Fisher Scientific). Ultraviolet-visible absorbance spectra were measured on a UV-2700 spectrometer (Shimadzu). Scanning electron microscopy (SEM) images were obtained by ZEISS Gemini 300. The X-ray diffraction (XRD) spectra were measured on a Shimadzu XRD-6100, using  $\text{Cu K}_\alpha$  ( $\lambda = 1.54056 \text{ \AA}$ ) radiation, an accelerating voltage of 40 kV, and an emission current of 30 mA.

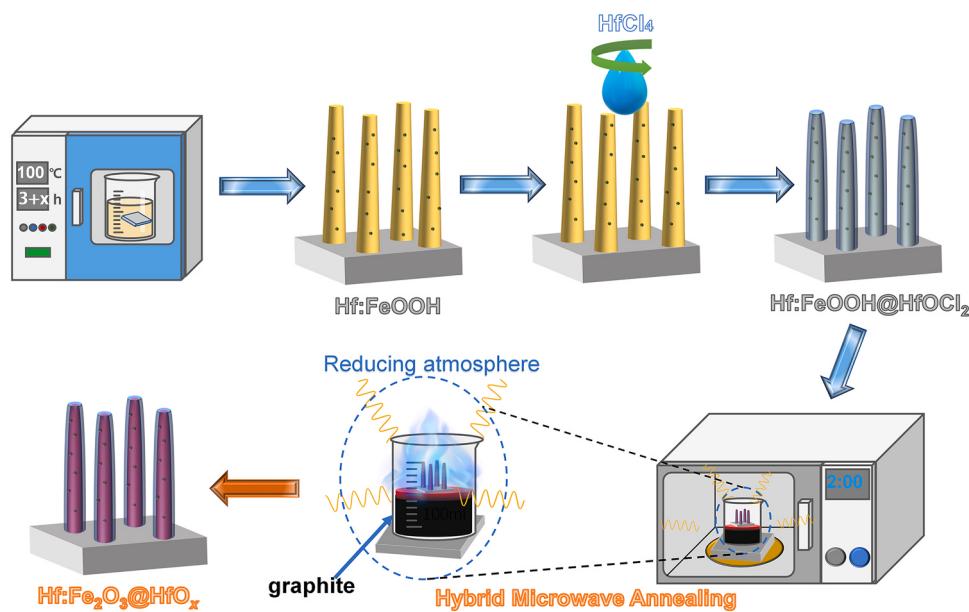
### 2.5. Photoelectrochemical measurements

The PEC performances were measured on a potentiostat (Iviumstat, h, Ivium Technologies) in a three-electrode system involving working electrode (the prepared photoanode with a  $1 \text{ cm}^2$  illuminated area), reference electrode ( $\text{Ag/AgCl}$ , 3.0 M KCl solution), and counter electrode (Pt) in a 1.0 M NaOH solution as an electrolyte.  $J$ - $V$  curves and photoelectrochemical impedance spectra (PEIS) were recorded under 1 sun ( $100 \text{ mW cm}^{-2}$ ) solar light generated by a solar simulator (Newport Sol 3 A with an AM 1.5 G filter), the intensity of which was calibrated with a standard silicon cell detector (Newport, PMKIT). All the measured potentials versus  $\text{Ag/AgCl}$  were converted to the potentials versus reversible hydrogen electrode using following equation:  $E_{\text{RHE}} = E_{\text{Ag/AgCl}} + 0.059 \text{ pH} + E_{\text{Ag/AgCl}}^0$  ( $E_{\text{Ag/AgCl}}^0 = 0.1976 \text{ at } 25^\circ\text{C}$ ). Linear sweep voltammetry (LSV) was measured in the range of 0.4–1.8  $\text{V}_{\text{RHE}}$  with a scan rate of  $0.02 \text{ V s}^{-1}$ . The Mott-Schottky plots were measured by sweeping 0.5–1.5  $\text{V}_{\text{RHE}}$  range with an alternative current (AC) frequency of 1000 Hz under the dark condition. The charge carrier density  $N_D$  was calculated by the equation:  $(\frac{A_s}{C_{\text{bulk}}})^2 = \frac{2}{\varepsilon \varepsilon_0 e N_D} (V - E_{FB} - \frac{k_B T}{e})$ , where  $(\frac{A_s}{C_{\text{bulk}}})$  is the surface area-corrected space charge capacitance,  $\varepsilon_0$  is the vacuum permittivity ( $8.85 \times 10^{-12} \text{ C}^2 \text{ J}^{-1} \text{ m}^{-1}$ ),  $\varepsilon$  is the dielectric constant of hematite (32),  $E_{FB}$  is the flat band potential,  $V$  is the applied voltage,  $e$  is electron charge ( $1.602 \times 10^{-19} \text{ C}$ ),  $k_B$  is Boltzmann constant ( $1.38 \times 10^{-23} \text{ J K}^{-1}$ ),  $T$  is the absolute temperature (298 K). PEIS spectra were recorded at  $1.23 \text{ V}_{\text{RHE}}$  with an AC potential frequency range of 100,000–0.1 Hz. A Z-View software (Scribner Associates) was used to fit the experimental PEIS data to an equivalent circuit model. The incident photon-to-electron conversion efficiency (IPCE) was measured using a 300 W Xe lamp equipped with AM 1.5 G filter and a monochromator (Newport, CS260B) with a bandwidth of 10 nm at  $1.23 \text{ V}_{\text{RHE}}$  in the same electrolyte. The incident photon-to-electro (IPCE) was calculated with the equation:  $\text{IPCE} = \frac{1240 \times J(\text{mA/cm}^2)}{P_{\text{light}}(\text{mW/cm}^2) \times \lambda(\text{nm})}$ , where  $J$  is the measured photocurrent density with a monochromator,  $P_{\text{light}}$  is the calibrated illumination power with a monochromator, and  $\lambda$  is the corresponding wavelength of the incident light.

## 3. Results and discussion

### 3.1. Fabrication and characterization of $\text{Hf:Fe}_2\text{O}_3 @\text{HfO}_x$ nanorods

The fabrication process of  $\text{Hf:Fe}_2\text{O}_3 @\text{HfO}_x$  nanorod photoanode is depicted in Scheme 1. First, in-situ Hf-doped  $\text{FeOOH}$  ( $\text{Hf:FeOOH}$ ) nanorods were grown on FTO by two consecutive steps of hydrothermal reaction to get a thick  $\text{Hf:FeOOH}$  film, which would improve the electronic conductivity of hematite by  $\text{Hf}^{4+}$  doping after conversion. Then, the  $\text{HfCl}_4$  solution was spin-coated on  $\text{Hf:FeOOH}$  to form an amorphous  $\text{HfOCl}_2$  layer. Subsequently, the prepared  $\text{Hf:FeOOH}@\text{HfOCl}_2$



**Scheme 1.** Schematic illustration for the synthesis of a  $\text{Hf:Fe}_2\text{O}_3 @\text{HfO}_x$  nanorod photoanode.

transformed into  $\text{Hf:Fe}_2\text{O}_3 @\text{HfO}_x$  by HMA, which accompanied a color change from yellow to dark red. Interestingly, the amorphous  $\text{HfO}_x$  layer formed on the nanorod surface displayed a hole storage capability instead of the well-known passivation effect as discussed below in detail. Note that the same  $\text{HfCl}_4$  precursor solution was used for both modifications.

SEM images of the  $\text{Hf:Fe}_2\text{O}_3$  film show the hematite nanorods of 650–800 nm long with diameters of 60–100 nm (Fig. S1), which are almost the same as the initial  $\text{Hf:FeOOH}$  nanorods before annealing (Fig. S2), confirming that HMA effectively maintained the original nanostructure. Besides, the surface of HMA-treated nanorods becomes smooth compared with  $\text{Hf:FeOOH}$ , suggesting that HMA not only converted  $\text{Hf:FeOOH}$  into  $\text{Hf:Fe}_2\text{O}_3$  phase, but reconfigured the surface structure [31]. After construction of surface  $\text{HfO}_x$  overlayer, the diameters of  $\text{Hf:Fe}_2\text{O}_3 @\text{HfO}_x$  are almost the same as the ones without  $\text{HfO}_x$  overlayer (Fig. 1a; Fig. S1a), which demonstrates a very thin  $\text{HfO}_x$  overlayer. Moreover, the energy dispersive X-ray (EDX) mapping shows the uniform distribution of O, Fe, and Hf elements in the nanorod, and sum spectrum reveals the clear existence of Hf element (Fig. S3).

The atomic structure of  $\text{Hf:Fe}_2\text{O}_3 @\text{HfO}_x$  was further examined by STEM. The HAADF-STEM image in Fig. 1c clearly shows a core-shell structure of the nanorod made of a 1–3 nm amorphous  $\text{HfO}_x$  shell and a highly crystalline  $\text{Hf:Fe}_2\text{O}_3$  core. The fast Fourier transforms (FFT) of two selected areas (Fig. S4) correspond to (110) plane of hematite with a *d*-spacing of 0.25 nm and (300) plane with a *d*-spacing of 0.15 nm, indicating that the significant incorporation of Hf atoms does not change the crystal structure of hematite, which is also supported by high resolution STEM in Fig. 1d. Many relatively larger bright points (dashed yellow circles) are observed clearly in hematite lattices, which are attributed to the substitutional Hf atoms. Besides, the EELS linear scanning (inset of Fig. 1d) clearly shows the high Hf concentrations in the shell and lower concentrations in the core with a modest gradient distribution, while Fe concentration displays exactly the reverse behavior. These results clearly verify the formation of  $\text{Hf:Fe}_2\text{O}_3 @\text{HfO}_x$  core-shell structure. In contrast,  $\text{Hf:Fe}_2\text{O}_3$  shows a uniform distribution of Hf, Fe, and O elements in EELS mapping images (Fig. S5), indicating that Hf element was uniformly doped into hematite lattices. Due to a small optimal concentration of  $\text{HfCl}_4$  and the limitation of spin-coating technique, there also exist some nanorods without  $\text{HfO}_x$  overlayer in  $\text{Hf:Fe}_2\text{O}_3 @\text{HfO}_x$  as shown in HAADF-STEM image in Fig. 1e, in which many bright points exist near the nanorod surface (within top ~3 nm

depth) ascribed to the substitutional Hf atoms [32,33]. These doped Hf atoms should have substituted into the Fe sites in (110) plane by HMA-induced rapid diffusion from the surface spin-coated  $\text{HfCl}_4$ . Moreover, the doped depth and area fluctuate at different surface locations, which is attributed to the fluctuation of local surface properties for the synthesized  $\text{Hf:FeOOH}$  nanorods. Our previous results demonstrated that the hydrophilic/hydrophobic surface (with/without oxygen plasma treatment) played an important role in the construction of shell structure during HMA [27,34]. The high-resolution STEM (HRSTEM) image shows a distinct feature of HAADF intensity, in which the bright points were identified as Hf atoms, while the light gray points in the background were ascribed to Fe atoms (Fig. 1f).

To further study local atomic arrangement of substitutional Hf atoms, a linescan for HAADF intensity was taken across the bright spots from surface to bulk, and the corresponding intensity data are plotted in the bottom of Fig. 1f. Clearly, the intensity of Hf atoms is much stronger than that of Fe atoms, and the average distance between two atoms is ~0.26 nm corresponding to the interatomic distance of Fe (110) plane [35], which in turn indicates that the substitution of Hf for Fe atoms does not change crystal lattices of hematite. Furthermore, the EELS mapping in Fig. 1g shows an inter-connected strong signal of Hf at the surface (white marked rectangle) relative to Fe and O signals, which is consistent with the ordered substitution of Hf for Fe atoms on the surface of nanorod (Fig. 1e). The blue marked area (inset of Fig. 1e) was transformed into inverse FFT image, which exhibits much clear difference between Hf and Fe atoms (Fig. 1h). Finally, the models of planar and three-dimensional structures are also constructed in Fig. 1i and j, respectively, which clearly display the atomic configuration of surface-doped structure.

The XRD patterns were used to analyze the crystallographic features of samples. Fig. 2a shows the similar XRD patterns with a strong peak intensity of (110) and weaker (104) and (012) peaks, which corresponds to the typical crystal structure of hematite (JCPDS no.33–0664) with no hafnium oxide impurity phases ( $\text{HfO}_2$ ,  $\text{FeHfO}$ ) [36]. Note that the half-width of (110) peak of  $\text{Hf:Fe}_2\text{O}_3 @\text{HfO}_x$  is a little larger than that of  $\text{Hf:Fe}_2\text{O}_3$ , implying that the  $\text{HfO}_x$  overlayer helps in maintaining a fine grain size of nanorods. More importantly, it has been proved that electron transport along (110) crystal plane is 4-orders of magnitude higher than that along (104) crystal plane [37]. In Fig. S6, the XRD of  $\text{Hf:Fe}_2\text{O}_3 @\text{HfO}_x$  prepared with 0.2 M  $\text{HfCl}_4$  solution shows specific peaks representing rhombohedral  $\alpha\text{-Fe}_2\text{O}_3$  and monoclinic  $\text{HfO}_2$  (JCPDS

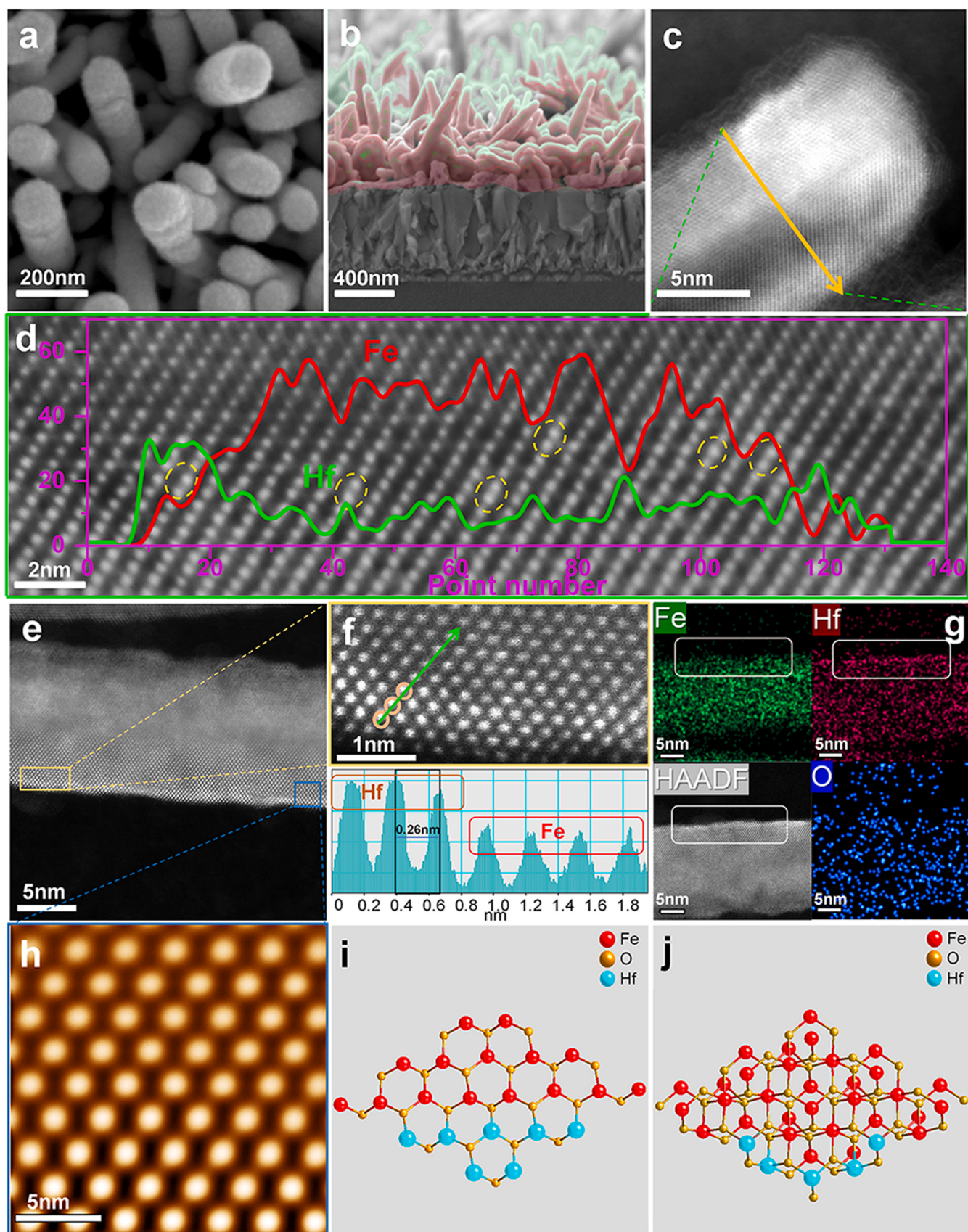


**Fig. 1.** Top and cross-section views of a, b) SEM, c) HAADF-STEM, d) HRSTEM (inset is the corresponding EELS linear scanning along the yellow arrow in (c) for Hf:Fe<sub>2</sub>O<sub>3</sub> @HfO<sub>x</sub> core-shell nanorods. The images of e) HAADF-STEM, f) HRSTEM (green line-scan for HAADF intensity analysis), g) EELS-mapping, h) corresponding inverse FFT, and i, j) monolayer and three-dimensional model simulation for a heavily surface-doped nanorod in the sample of Hf:Fe<sub>2</sub>O<sub>3</sub> @HfO<sub>x</sub>.

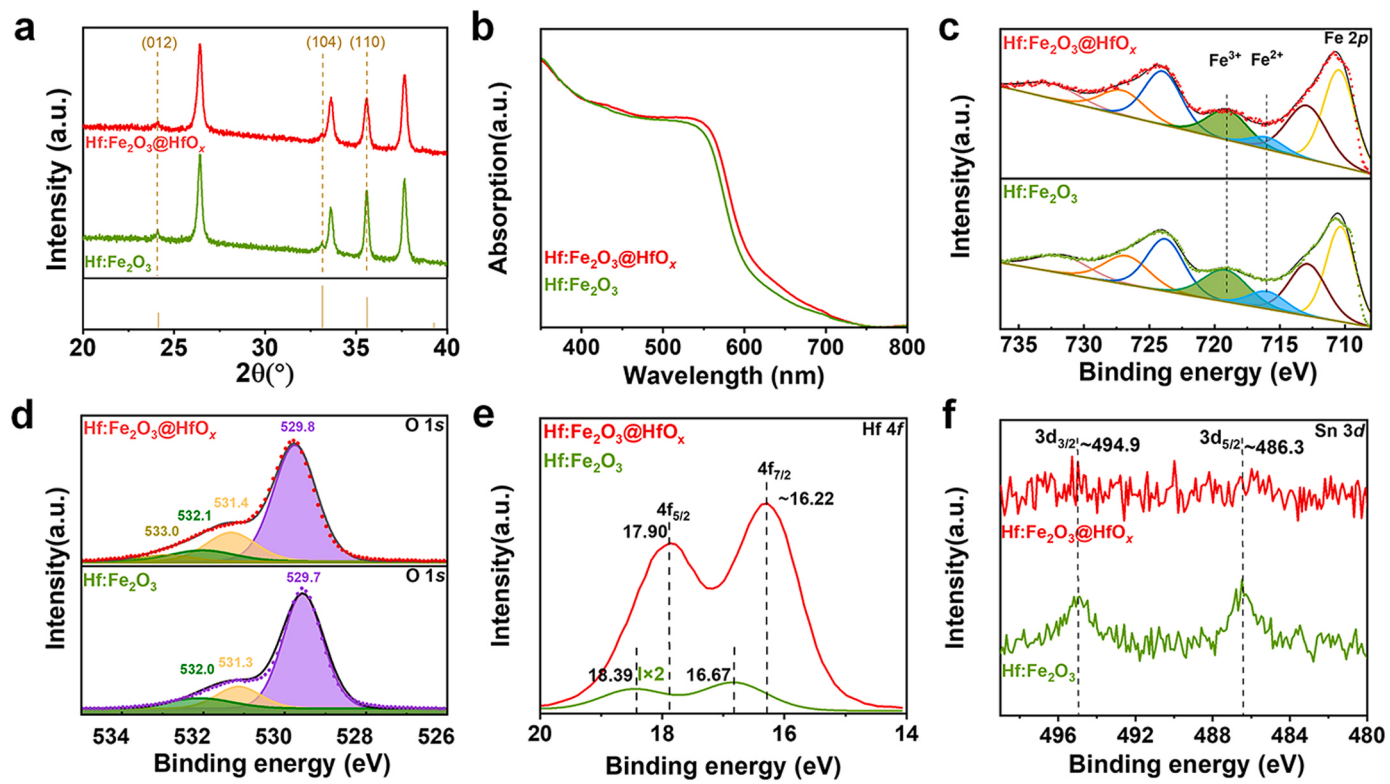


Fig. 2. (a) XRD patterns, (b) UV-vis absorption spectra, and XPS spectra of  $\text{Hf:Fe}_2\text{O}_3$ , and  $\text{Hf:Fe}_2\text{O}_3 @\text{HfO}_x$ . (c)  $\text{Fe}\ 2p$ . (d)  $\text{O}\ 1s$ . (e)  $\text{Hf}\ 4f$ . (f)  $\text{Sn}\ 3d$ .

no.43–1017), indicating that the crystalline  $\text{HfO}_2$  phase becomes visible as the concentration of  $\text{HfCl}_4$  increases. However, the photocurrent density decreases rapidly with an increase of crystalline  $\text{HfO}_2$  (Fig. S7). In contrast, when 0.05 M  $\text{HfCl}_4$  was used, the complete absence of crystalline  $\text{HfO}_2$  was observed, indicating it is in amorphous state, which is consistent with the above HRTEM result (Fig. 1c).

The UV-vis absorption spectra (Fig. 2b) were measured to evaluate the light harvesting capability.  $\text{Hf:Fe}_2\text{O}_3 @\text{HfO}_x$  improves light absorption slightly relative to that of  $\text{Hf:Fe}_2\text{O}_3$  owing to considerable substitution of Hf atoms (Fig. 1e, f) and external coating by the  $\text{HfO}_x$  overlayer (Fig. 1c). From the Tauc plots (Fig. S8),  $\text{Hf:Fe}_2\text{O}_3 @\text{HfO}_x$  ( $\sim 2.07$  eV) shows a smaller bandgap relative to that of  $\text{Hf:Fe}_2\text{O}_3$  ( $\sim 2.09$  eV), implying that more Hf dopants indeed decrease the band gap of hematite by generating impurity energy level.

The valence state and chemical composition of each element were examined by XPS (Fig. S9). The  $\text{Fe}\ 2p$  spectra in Fig. 2c can be deconvoluted into two main peaks with binding energies (BEs) of 724.08 eV and 710.28 eV corresponding to  $\text{Fe}\ 2p_{1/2}$  and  $2p_{3/2}$  spin-orbit split peaks of  $\text{Fe}_2\text{O}_3$ , respectively [38]. The satellite peak at  $\sim 719$  eV for the  $\text{Fe}^{3+}$  species is similar for both samples, while another weak satellite peak at  $\sim 716$  eV for the  $\text{Fe}^{2+}$  species shows clear differences [34]. The  $\text{Fe}^{2+}$  satellite peak of  $\text{Hf:Fe}_2\text{O}_3 @\text{HfO}_x$  becomes very weak owing to formation of the  $\text{HfO}_x$  overlayer, which protects hematite nanorods from losing oxygen atoms by reductive atmosphere of HMA.

The  $\text{O}\ 1s$  XPS spectra in Fig. 2d can be deconvoluted into three or four individual peaks corresponding to lattice oxygen ( $\text{O}_1$ , 529.7–530.2 eV), oxygen vacancy ( $\text{O}_v$ , 531.2–531.6 eV), and adsorbed oxygen/surface hydroxyl groups ( $\text{O}_{\text{ad}}/(\text{OH})_{\text{ad}}$ , 532.0–533.0 eV) [39]. In fact, both HMA and  $\text{Hf}^{4+}$  ion doping could lead to  $\text{O}_v$  formation effectively. The substitution of  $\text{Hf}^{4+}$  for  $\text{Fe}^{3+}$  ions in hematite provides additional electron relocation and generates  $\text{Fe}^{2+}$  ions, which would accompany the formation of  $\text{O}_v$  for charge compensation [40]. Clearly,  $\text{Hf:Fe}_2\text{O}_3 @\text{HfO}_x$  shows a higher  $\text{O}_v$  concentration compared to  $\text{Hf:Fe}_2\text{O}_3$  due to the weaker Hf–O bonds of amorphous  $\text{HfO}_x$  overlayer. The results are consistent with the analysis of  $\text{Fe}^{2+}$  satellite peaks (Fig. 2c). It

should be noted that a proper concentration of  $\text{O}_v$  in hematite is beneficial for high PEC performance [41]. Moreover,  $\text{O}_{\text{ad}}/(\text{OH})_{\text{ad}}$  signal can be observed notably in  $\text{Hf:Fe}_2\text{O}_3 @\text{HfO}_x$ , and these hydrophilic groups tend to shift the location of surface states negatively to improve OER [42].

In Fig. 2e,  $\text{Hf}\ 4f$  XPS spectra of  $\text{Hf:Fe}_2\text{O}_3$  show a doublet peak at  $\sim 16.67$  eV and  $\sim 18.39$  eV belonging to  $\text{Hf}\ 4f_{7/2}$  and  $\text{Hf}\ 4f_{5/2}$  orbitals of  $\text{Hf}(\text{IV})$  state [27,28,43], which can improve the conductivity of hematite by donating additional electrons. In contrast, the BEs of those peaks in  $\text{Hf:Fe}_2\text{O}_3 @\text{HfO}_x$  show a negative shift by  $\sim 0.4$  eV to  $\sim 16.22$  eV and  $\sim 17.90$  eV with respect to that of  $\text{Hf:Fe}_2\text{O}_3$ , which indicates a lower oxidation state of Hf ( $<+4$ ) in amorphous  $\text{HfO}_x$  shell. Undoubtedly, this behavior is related to the unique feature of reductive atmosphere induced by HMA, which leads to the generation of oxygen vacancies ( $\text{O}_v$ ). The oxidation state of Fe could be reduced more easily in  $\text{Hf:Fe}_2\text{O}_3$  to form  $\text{Fe}^{2+}$  ions since Hf–O bond is stronger than Fe–O bond [44]. In  $\text{Hf:Fe}_2\text{O}_3 @\text{HfO}_x$ , however,  $\text{HfO}_x$  shell is exposed to the reducing atmosphere of HMA cell and is readily reduced, while  $\text{Hf:Fe}_2\text{O}_3$  core would preserve oxygen atoms effectively due to protection by the  $\text{HfO}_x$  shell. These results are in agreement with  $\text{Fe}^{2+}$  satellite peaks (Fig. 2c) and generation of  $\text{O}_v$  (Fig. 2d). However, the substitutionally-doped Hf atoms on the surface still undergo reduction of Hf–O bonds due to the localized non-uniformity of the reductive atmosphere. Certainly,  $\text{Hf:Fe}_2\text{O}_3 @\text{HfO}_x$  shows a higher Hf signal intensity owing to the  $\text{HfO}_x$  shell. It should be noted that a lower valence state of Hf in amorphous  $\text{HfO}_x$  shell is ready to extract and store the photo-generated holes from the core of  $\text{Hf:Fe}_2\text{O}_3$  nanorods (discussed below).

Fig. 2f shows Sn 3d XPS peaks centered at  $\sim 486.3$  eV ( $\text{Sn}\ 3d_{5/2}$ ) and  $\sim 494.9$  eV ( $\text{Sn}\ 3d_{3/2}$ ) corresponding to BEs of  $\text{SnO}_2$ , indicating that  $\text{Sn}^{4+}$  ions were unintentionally doped into  $\text{Hf:Fe}_2\text{O}_3$  nanorods from the FTO substrate during the process of HMA [16]. Obviously,  $\text{Hf:Fe}_2\text{O}_3$  shows a weak Sn signal owing to Hf doping, while Sn signal disappears in  $\text{Hf:Fe}_2\text{O}_3 @\text{HfO}_x$  due to significant additional obstruction of Sn diffusion by counter diffusion of Hf from the  $\text{HfO}_x$  shell.

### 3.2. Photoelectrochemical performance

The PEC water splitting performance of the prepared photoanodes was studied under simulated 1 sun irradiation ( $100 \text{ mW cm}^{-2}$ ) with an AM 1.5 G filter in 1 M NaOH electrolyte in a three-electrode cell with the photoanode, Ag/AgCl (3.0 M KCl), and Pt plate as working, reference, and counter electrodes, respectively (Fig. S10). Fig. 3a shows the photocurrent-potential ( $J-V$ ) curves for hematite photoanodes with different modifications. The pristine  $\alpha\text{-Fe}_2\text{O}_3$  photoanode showed a typical photo-response with a photocurrent density of  $1.27 \text{ mA cm}^{-2}$  at  $1.23 \text{ V}_{\text{RHE}}$ . The Hf:Fe<sub>2</sub>O<sub>3</sub> photoanode was optimized with respect to the Hf dopant concentration (Fig. S11) and the condition of the double hydrothermal growth (re-growth) (Fig. S12), which thus generates a remarkable  $J_{\text{ph}}$  of  $1.81 \text{ mA cm}^{-2}$  at  $1.23 \text{ V}_{\text{RHE}}$  under the standard conditions. With additional modification of HfO<sub>x</sub> overlayer,  $J_{\text{ph}}$  is further enhanced to  $3.47 \text{ mA cm}^{-2}$  at  $1.23 \text{ V}_{\text{RHE}}$  (Fig. S7), which is almost  $\sim 2$  times that of the optimized Hf:Fe<sub>2</sub>O<sub>3</sub>. Besides, the  $J_{\text{ph}}$  reaches  $5.53 \text{ mA cm}^{-2}$  at  $1.60 \text{ V}_{\text{RHE}}$  where the dark current begins to take off, indicative of a large fill factor. The performance is superior to the recently reported state-of-the-art hematite-based photoanodes without co-catalyst (Table S2). When CTA method was employed instead of HMA for the photoanode fabrication (Figs. S13 and S14),  $\alpha\text{-Fe}_2\text{O}_3$  shows a modest  $J_{\text{ph}}$  of  $0.93 \text{ mA cm}^{-2}$  at  $1.23 \text{ V}_{\text{RHE}}$  even though the same FeOOH precursor film was used as for HMA. Both Hf doping and HfO<sub>x</sub> overlayer show the expected promotional effects, making  $J_{\text{ph}}$  increase to  $1.38 \text{ mA cm}^{-2}$  and  $1.63 \text{ mA cm}^{-2}$  at  $1.23 \text{ V}_{\text{RHE}}$  sequentially, yet they are still less than a half of the performance of the corresponding photoanodes fabricated by HMA. The results highlight the superiority of HMA in fabricating high-efficiency photoelectrodes.

The onset potential ( $V_{\text{on}}$ ) is another important figure of merit for photoanodes. It was evaluated by two ways (Fig. S15), both showing the similar values of  $0.79$ ,  $0.87$  and  $0.85 \text{ V}_{\text{RHE}}$  for Fe<sub>2</sub>O<sub>3</sub>, Hf:Fe<sub>2</sub>O<sub>3</sub>, and Hf:Fe<sub>2</sub>O<sub>3</sub>@HfO<sub>x</sub>, respectively. Normally, doped metal ions form carrier

centers, which may increase the  $V_{\text{on}}$  of OER, while HfO<sub>x</sub> overlayer shows a little decrease of  $V_{\text{on}}$  owing to the typical surface passivation effect. The  $E_{\text{FB}}$  and  $N_{\text{D}}$  were derived from Mott-Schottky plots (Fig. S16). Clearly, both Hf-doped photoanodes (Hf:Fe<sub>2</sub>O<sub>3</sub>, Hf:Fe<sub>2</sub>O<sub>3</sub>@HfO<sub>x</sub>) show obvious decreases of the slope from that of bare hematite, indicating significant increases in donor densities [45]. Note that Hf:Fe<sub>2</sub>O<sub>3</sub>@HfO<sub>x</sub> shows an almost parallel slope with respect to that of Hf:Fe<sub>2</sub>O<sub>3</sub>, indicating that the HfO<sub>x</sub> overlayer does not contribute much to increased  $N_{\text{D}}$ . It is against expectation because the HfO<sub>x</sub> overlayer could provide additional Hf dopants to Fe<sub>2</sub>O<sub>3</sub>. But protection by the HfO<sub>x</sub> overlayer suppresses the formation of surface oxygen vacancy ( $\text{O}_v$ ) in hematite (another source of charge carriers), which would offset the contribution from the HfO<sub>x</sub> shell. Of course, the generated  $\text{O}_v$  in HfO<sub>x</sub> overlayer itself by HMA would not contribute to the  $N_{\text{D}}$  of hematite. However,  $E_{\text{FB}}$  shows a difference of  $\sim 100 \text{ mV}$  owing to generation of more surface states and  $\text{O}_v$  by Hf doping in Hf:Fe<sub>2</sub>O<sub>3</sub> sample, while Hf:Fe<sub>2</sub>O<sub>3</sub>@HfO<sub>x</sub> shifts  $E_{\text{FB}}$  negatively because of the passivation effect and additional Hf doping at  $1\text{--}2 \text{ nm}$  depth of the hematite surface due to the HfO<sub>x</sub> overlayer (Fig. 1e). These results are in agreement with the behavior of  $V_{\text{on}}$  (Fig. S15).

A most significant discovery of the current work is the hole-storage capability of the amorphous HfO<sub>x</sub> overlayer. Transient photocurrent measurements under chopped illumination in Fig. 3b exhibit anodic/cathodic current spikes upon light on/off, which indicates that the photogenerated holes are accumulated at the photoanode|electrolyte interface, and would in turn take part in recombination with conduction band electrons [46,47]. Compared with the photoanodes without HfO<sub>x</sub> overlayer, the Hf:Fe<sub>2</sub>O<sub>3</sub>@HfO<sub>x</sub> photoanode shows prominent current spikes at the potential range of  $0.8\text{--}1.3 \text{ V}_{\text{RHE}}$  both on light and in dark, suggesting that HfO<sub>x</sub> overlayer serves the hole storage function. Thus, the HfO<sub>x</sub> overlayer as a hole-storage layer could promote sluggish water oxidation kinetics, yet it can also lead to high possibility of recombination with conduction band electrons and back reaction (oxygen

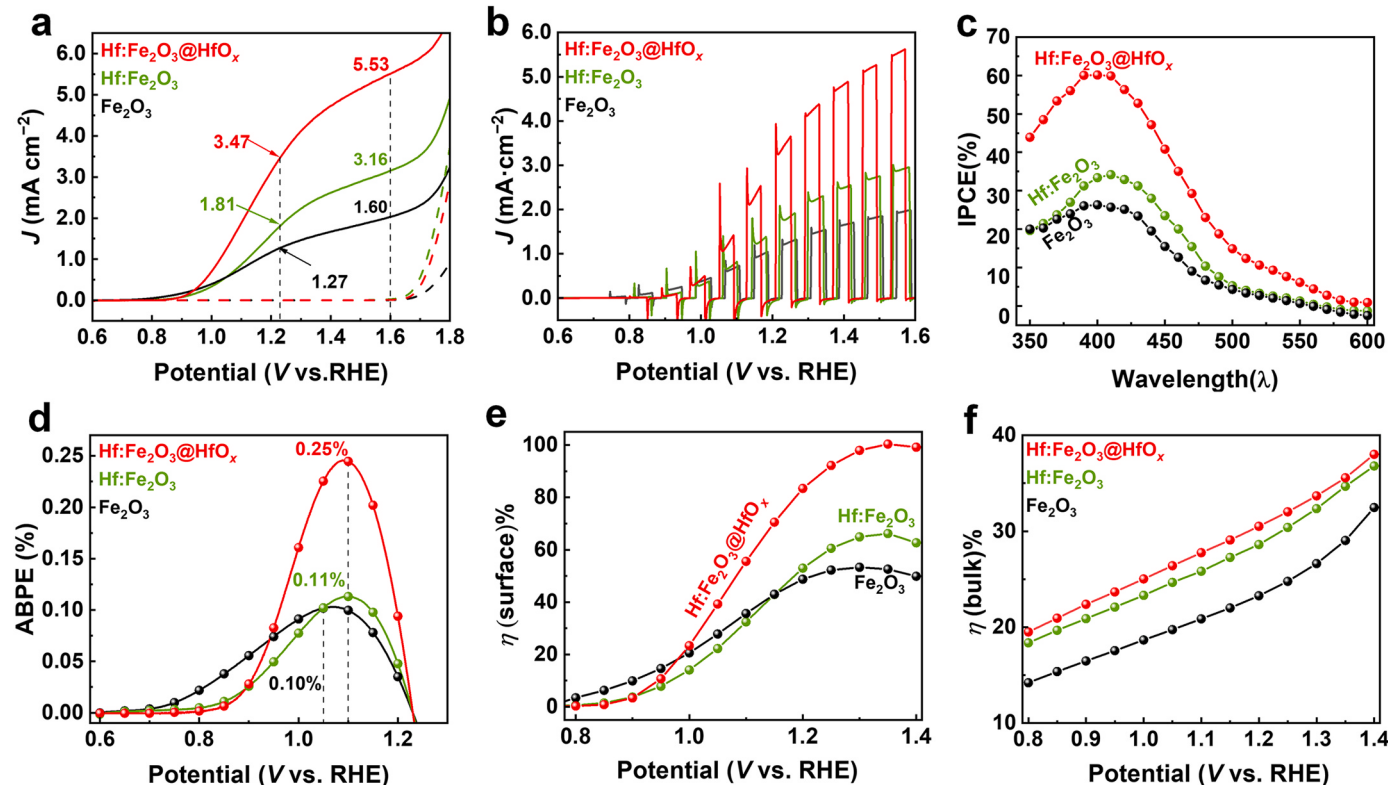


Fig. 3. Photoelectrochemical performance of Fe<sub>2</sub>O<sub>3</sub>, Hf:Fe<sub>2</sub>O<sub>3</sub>, and Hf:Fe<sub>2</sub>O<sub>3</sub>@HfO<sub>x</sub> photoanodes a)  $J-V$  curves, b) chopped  $J-V$  curves, c) IPCE, d) ABPE, e) surface charge separation efficiency ( $\eta(\text{surface})$ ), f) bulk charge separation efficiency ( $\eta(\text{bulk})$ ).

reduction) owing to the extended lifetime of holes [48]. The latter negative effect can be mitigated by an effective OER co-catalyst as discussed later. Interestingly, HMA-treated  $\text{Hf:Fe}_2\text{O}_3 @\text{HfO}_x$  shows stronger anodic and cathodic current spikes from 0.8 V to 1.3 V<sub>RHE</sub> in comparison with the same photoanode treated with CTA (Fig. S17a), indicating that HMA treatment could generate high hole-storage capability owing to its unique feature of reductive atmosphere. Besides, the surface charge separation efficiency ( $\eta_{\text{surface}}$ ) of HMA-treated photoanode is substantially higher than that of CTA-treated photoanode (Fig. S17b), suggesting that the  $\text{HfO}_x$  overlayer formed by HMA could extract more efficiently the photogenerated holes from  $\text{Hf:Fe}_2\text{O}_3$  nanorods and thereby promote the sluggish OER kinetics significantly using the accumulated/stored holes.

To explore the essential roles played by Hf doping and the  $\text{HfO}_x$  overlayer, PEIS was employed to study the charge transfer behaviors of prepared photoanodes. Representative two-RC-units equivalent circuit models were used to fit data obtained for Nyquist plots of  $\text{Fe}_2\text{O}_3$ ,  $\text{Hf:Fe}_2\text{O}_3$ , and  $\text{Hf:Fe}_2\text{O}_3 @\text{HfO}_x$  photoanodes (Fig. S18). The PEIS Nyquist plots were well-fitted using both circuit models and the detailed fitting values are listed in Table S3. The radii of semicircles (or the resistances) decrease gradually with additional modifications:  $\text{Fe}_2\text{O}_3 > \text{Hf:Fe}_2\text{O}_3 > \text{Hf:Fe}_2\text{O}_3 @\text{HfO}_x$ . The charge transfer resistance ( $R_{\text{ct}}$ ) of the  $\text{Hf:Fe}_2\text{O}_3 @\text{HfO}_x$  photoanode from the surface to electrolyte is significantly smaller than those of the others. However, its bulk resistance ( $R_{\text{trap}}$ ) is commensurate with that of  $\text{Hf:Fe}_2\text{O}_3$  owing to effective Hf doping for both photoanodes. On the other hand, the capacitance associated with surface states ( $C_{\text{ss}}$ ) shows a large increase with decoration of  $\text{HfO}_x$  overlayer onto  $\text{Hf:Fe}_2\text{O}_3$ , which indicates that the extraction and storage capacity of photogenerated holes increases markedly [21].

The IPCE measured under 1 sun illumination (Fig. S19) is significantly enhanced by Hf doping and hole-storage layer (HSL) over the entire photon energy until it approaches zero at the band gap of hematite ( $\lambda \sim 600$  nm). In particular, IPCE of  $\text{Hf:Fe}_2\text{O}_3 @\text{HfO}_x$  shows 15–25 % improvement relative to that of  $\text{Hf:Fe}_2\text{O}_3$  in a wavelength range of 350–450 nm, indicating outstanding ability of solar photon conversion (Fig. 3c). Moreover, the integrated IPCE with reference to AM 1.5 G spectrum at 1.23 V<sub>RHE</sub> gives a solar photocurrent ( $J_{\text{SC}}$ ) of 1.27, 1.73, and 3.43 mA cm<sup>-2</sup> for  $\text{Fe}_2\text{O}_3$ ,  $\text{Hf:Fe}_2\text{O}_3$ , and  $\text{Hf:Fe}_2\text{O}_3 @\text{HfO}_x$ , respectively (Fig. S20), which are very close to the experimentally measured  $J_{\text{ph}}$  values at 1.23 V<sub>RHE</sub> (Fig. 3a). Taken all these together, the enhanced IPCE by Hf doping and  $\text{HfO}_x$  overlayer is indeed due to the improved charge separation and hole-storage capability, respectively. The applied-bias photon-to-current conversion efficiency ( $\text{ABPE} = J_{\text{ph}} \times (1.23 - E) / P_{\text{irradiation}}$ ) represents the net effect of photoelectrode by subtracting the contribution of bias potential (E). Fig. 3d shows increasing peak ABPE values in order of  $\text{Hf:Fe}_2\text{O}_3 @\text{HfO}_x$  (0.25 % at 1.10 V<sub>RHE</sub>) >  $\text{Hf:Fe}_2\text{O}_3$  (0.11 % 1.10 V<sub>RHE</sub>) >  $\text{Fe}_2\text{O}_3$  (0.10 % 1.05 V<sub>RHE</sub>).

Bulk charge separation efficiency ( $\eta_{\text{bulk}}$ ) and surface charge injection efficiency ( $\eta_{\text{surface}}$ ) were determined in the same electrolyte with addition of 0.5 M  $\text{H}_2\text{O}_2$  as a hole scavenger, as described in Fig. S21 [49]. The  $\eta_{\text{bulk}}$  denotes the fraction of photogenerated holes that reach the photoanode surface without recombination in the bulk of photoanode, while  $\eta_{\text{surface}}$  represents the fraction of those surface holes that are injected to the water oxidation successfully. In Fig. 3e,  $\eta_{\text{surface}}$  values are similar for  $\text{Fe}_2\text{O}_3$  and  $\text{Hf:Fe}_2\text{O}_3$ , but  $\text{Hf:Fe}_2\text{O}_3 @\text{HfO}_x$  shows a greatly increased  $\eta_{\text{surface}}$  at potential range of 1.0–1.6 V<sub>RHE</sub> owing to the efficient hole-storage capability of  $\text{HfO}_x$  layer. Interestingly, its  $\eta_{\text{surface}}$  value reaches near 100 % at ~1.3 V<sub>RHE</sub>, indicating that the fraction of surface holes not yet participated in the reaction would be stored in the  $\text{HfO}_x$  layer temporarily instead of recombination with electrons, consequently making full use of holes that reached the surface, which is consistent with the previous reports [50,51]. In Fig. 3f,  $\eta_{\text{bulk}}$  of  $\text{Hf:Fe}_2\text{O}_3$  shows a significant improvement relative to that of  $\text{Fe}_2\text{O}_3$  starting from 0.8 V<sub>RHE</sub>, indicating that Hf doping could effectively reduce bulk charge recombination by introduction of high valent ions [52,53]. However, the hole-storage layer of  $\text{HfO}_x$  improves  $\eta_{\text{bulk}}$  to a limited extent because the

electrical conductivity of hematite nanorods is already well-improved by initial in-situ Hf doping. It should be noted that the surface overlayer of  $\text{HfO}_x$  selectively extracts/stores photogenerated holes from the bulk of  $\text{Hf:Fe}_2\text{O}_3$ , thus significantly improving both bulk and surface charge separation efficiencies.

The capacity of hole storage can be quantified from the photocurrent response under chopped light illumination. By integrating the photocurrent transient peak, the amount of charge storage can be determined by the passed charges during the surface recombination process [54]. In Fig. S22, it is obvious that the quantity of holes stored in  $\text{Hf:Fe}_2\text{O}_3 @\text{HfO}_x$  increases with applied potential compared with  $\text{Hf:Fe}_2\text{O}_3$  and  $\text{Fe}_2\text{O}_3$  photoanodes (Fig. 4a), while the quantities show a little increase for  $\text{Hf:Fe}_2\text{O}_3$  compared to  $\text{Fe}_2\text{O}_3$ . Moreover, the HMA-treated  $\text{Hf:Fe}_2\text{O}_3 @\text{HfO}_x$  shows vastly higher hole-storage capacity than CTA-treated one (Fig. S23). All the above results demonstrate that HMA could form a more effective  $\text{HfO}_x$  hole-storage layer.

In order to verify whether the surface hole-extraction/storage layer can appear on all photoanodes,  $\text{HfCl}_4$  solutions with different concentrations were spin-coated on the surface of pristine  $\text{FeOOH}$  nanorods directly. This is the usual procedure to prepare ex-situ doped hematite photoanodes. The optimized photoanode achieves an improved current density  $J_{\text{ph}}$  of 2.21 mA cm<sup>-2</sup> at 1.23 V<sub>RHE</sub> (Fig. S24a), but the current spikes of chopped J-V curves for pristine  $\text{Fe}_2\text{O}_3$  and ex-situ Hf-doped  $\text{Fe}_2\text{O}_3$  (ex- $\text{Hf:Fe}_2\text{O}_3$ ) are similar (Fig. S24b). The result suggests that the spin-coating of  $\text{HfCl}_4$  solution on pristine  $\text{FeOOH}$  mainly results in Hf-doping instead of forming a hole-storage layer. This is further supported by the Mott-Schottky plot, which shows the doubled  $N_{\text{D}}$  of ex-Hf:  $\text{Fe}_2\text{O}_3$  relative to that of pristine  $\text{Fe}_2\text{O}_3$  (Fig. S24c). Note that  $N_{\text{D}}$  shows almost no increase from  $\text{Hf:Fe}_2\text{O}_3$  to  $\text{Hf:Fe}_2\text{O}_3 @\text{HfO}_x$  (Fig. S16) as discussed before. The results demonstrate that only when the amount of pre-doped Hf is sufficient, the spin-coated  $\text{Hf}^{4+}$  ions could be effectively prevented from entering hematite lattices and instead form a thin amorphous  $\text{HfO}_x$  layer on the surface.

In addition to chopped-light J—V curves and PEIS, cathodic discharge measurements (CDM) can also be used to investigate the surface trapped holes [55,56]. In CDM sequence (detailed description in Fig. S25), the sample is first pre-oxidized by applying sufficient anodic bias (1.6 V<sub>RHE</sub>) under illumination so as to drive water photo-oxidation and oxygen evolution. Then, the amount of charge stored in oxidized intermediates could be evaluated by the potentiodynamic discharge characteristics upon turning the light off by sweeping the potential cathodically [57]. The current responses of the photoanodes to the changes in illumination and potential conditions are shown in Fig. 4b. At a high intermediate potential ( $V_{\text{int}}$ , 1.3 V<sub>RHE</sub>), the size of discharge wave for  $\text{Hf:Fe}_2\text{O}_3$  indicates equivalent surface trapped holes or oxidized intermediates in the discharge time of 1.5–3.5 s. However,  $\text{Hf:Fe}_2\text{O}_3 @\text{HfO}_x$  in this period shows a relatively larger and delayed discharge wave, indicating that a larger amount of surface stored holes or oxidized intermediates take a longer time to reach the recombinational potential. At a middle  $V_{\text{int}}$  (1.0 V<sub>RHE</sub>), the discharge wave appears in earlier period of 1.0–2.0 s, and the size follows the order of  $\text{Hf:Fe}_2\text{O}_3 @\text{HfO}_x > \text{Hf:Fe}_2\text{O}_3 > \text{Fe}_2\text{O}_3$ , suggesting that  $\text{HfO}_x$  overlayer effectively influences the potentiodynamic discharge of oxidized intermediates. At a low  $V_{\text{int}}$  (0.8 V<sub>RHE</sub>), the discharge waves of  $\text{Hf:Fe}_2\text{O}_3$  disappear completely, while  $\text{Hf:Fe}_2\text{O}_3 @\text{HfO}_x$  still maintains a trace of discharge wave in the period of 0.9–1.5 s, indicating an outstanding hole-storage capability of  $\text{HfO}_x$  overlayer. Moreover, the capacitive spike of  $\text{Hf:Fe}_2\text{O}_3 @\text{HfO}_x$  in the period of 0.0–0.2 s is the largest, indicating the largest amount of discharged holes or oxidized intermediates (Fig. 4c). On the other hand, as the lower the applied potential is, the lower is the energy band bending towards the surface, consequently facilitating surface-trapped holes to combine with electrons. Definitely, the more driving force is required for  $\text{Hf:Fe}_2\text{O}_3 @\text{HfO}_x$  to achieve a complete discharge of the stored holes (recombination with electrons) owing to the high hole storage capacity of the amorphous  $\text{HfO}_x$  overlayer.

In a 4 h stability test (Fig. 4d),  $\text{Fe}_2\text{O}_3$  and  $\text{Hf:Fe}_2\text{O}_3$  show the stability

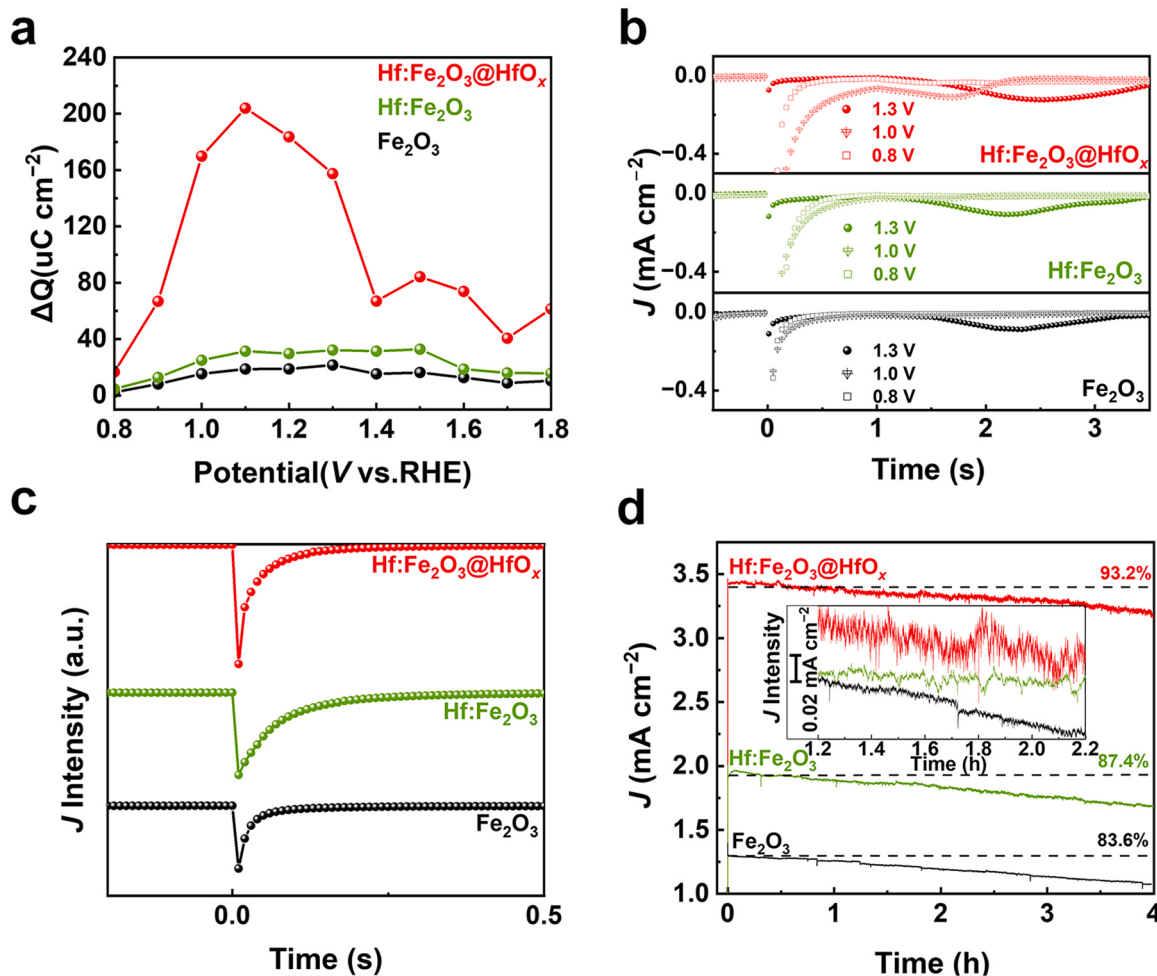


**Fig. 4.** Photoelectrochemical performance of  $\text{Fe}_2\text{O}_3$ ,  $\text{Hf:Fe}_2\text{O}_3$ , and  $\text{Hf:Fe}_2\text{O}_3 @\text{HfO}_x$  photoanodes; a) hole storage capacity, b) capacitive spike at 0.0–0.2 s with  $V_{\text{int}} = 0.80 \text{ V}_{\text{RHE}}$ , c) cathodic discharge measurement, and d) stability test.

by losing  $\sim 16\%$  and  $\sim 13\%$  of the original photocurrents. However,  $\text{Hf:Fe}_2\text{O}_3 @\text{HfO}_x$  improves the stability by limiting photocurrent decay less than  $\sim 7\%$ , which results from surface protection capability of  $\text{HfO}_x$  overlayer by the large dissociation energy of  $\text{Hf}–\text{O}$  bonds. In particular, the amplitude variation of photocurrent density for  $\text{Hf:Fe}_2\text{O}_3 @\text{HfO}_x$  is larger than those of  $\text{Fe}_2\text{O}_3$  and  $\text{Hf:Fe}_2\text{O}_3$  (inset of Fig. 4d), probably reflecting the dynamic processes of holes extraction, storage, and release in the  $\text{HfO}_x$  overlayer.

Although surface and bulk hafnium engineering brought markedly improved PEC performance of hematite photoanode, we applied an additional modification strategy. Thus,  $\text{NiCoFe(OH)}_x$ , a representative OER co-catalyst was deposited on the surface of  $\text{Hf:Fe}_2\text{O}_3 @\text{HfO}_x$  photoanode [58]. With  $\text{NiCoFe(OH)}_x$  loading under optimized conditions (Fig. S26),  $J_{\text{ph}}$  is further enhanced to  $4.13 \text{ mA cm}^{-2}$  at  $1.23 \text{ V}_{\text{RHE}}$  with cathodic shifting of  $V_{\text{on}}$  by  $60 \text{ mV}$  (Fig. S27a,b) [59]. Besides, the photocurrent spikes are obviously decreased with the co-catalyst (Fig. S27c), suggesting that  $\text{NiCoFe(OH)}_x$  can effectively transfer the holes stored in the  $\text{HfO}_x$  overlayer to participate in water oxidation, thus accelerating the slow kinetics of OER [9]. The results demonstrate a highly interesting and beneficial synergistic effect of a high hole storage/extraction capability of the  $\text{HfO}_x$  overlayer and fast injection of the holes into the electrolyte by the  $\text{NiCoFe(OH)}_x$  co-catalyst to promote efficient OER [22]. Moreover, the stability is further improved to  $98.9\%$  in a 4 h test (Fig. S28d), which is significantly better than that of  $\text{Hf:Fe}_2\text{O}_3 @\text{HfO}_x$  ( $93.2\%$ ).

#### 4. Conclusions

We have demonstrated a distinctive strategy of HMA-induced hafnium engineering to boost the PEC performance of hematite, which involves two aspects of the bulk and surface: in-situ hafnium doping into the hematite lattice and the formation of amorphous  $\text{HfO}_x$  overlayer. In particular, HMA-induced amorphous  $\text{HfO}_x$  overlayer was found to display a distinctive function of hole storage, which promotes charge separation very efficiently. This effect by an amorphous  $\text{HfO}_x$  overlayer has never been reported before. The formation and functions of the hole-storage layer of amorphous  $\text{HfO}_x$  were unambiguously elucidated by multiple techniques, including HRTEM, chopped  $J–V$  curves, PEIS, CDM, and near  $100\% \eta_{\text{surface}}$ . In contrast, CTA-treated hematite photoanode did not show the hole-storage function of  $\text{HfO}_x$  overlayer, and its  $J_{\text{ph}}$  was very low, which highlights the unique efficacy of HMA. Consequently, the fabricated  $\text{Hf:Fe}_2\text{O}_3 @\text{HfO}_x$  photoanode achieved a high  $J_{\text{ph}}$  of  $3.47 \text{ mA cm}^{-2}$  at  $1.23 \text{ V}_{\text{RHE}}$  under simulated 1-sun illumination. Moreover,  $\text{NiCoFe(OH)}_x$  cocatalyst modification demonstrated a synergistic promotional effect with the hole-storage function of  $\text{HfO}_x$  overlayer, recording  $J_{\text{ph}}$  of  $4.13 \text{ mA cm}^{-2}$  at  $1.23 \text{ V}_{\text{RHE}}$ , which is 3 times higher than that of pristine  $\text{Fe}_2\text{O}_3$  photoanode ( $1.24 \text{ mA cm}^{-2}$ ). The performance is comparable to the state-of-the-art hematite photoanodes reported recently.

## Supporting Information

The **Supporting Information** is available free of charge on the website at Synthesized process scheme, surface morphologies of SEM images, EDX-SEM images, HRTEM images, XRD pattern, XPS survey spectra,  $J$ – $V$  curves for optimization of  $\text{HfCl}_4$  concentration and cocatalyst amount,  $J$ – $V$  curves for bare hematite by HMA and CTA.

## CRediT authorship contribution statement

**Weicong Li:** Conceptualization, Investigation, Writing - original draft. **Hongying Guo:** Investigation. **Chenyang Xu:** Validation, Formal analysis. **Chenke Tang:** Data curation, Software. **Jae Sung Lee:** Writing – review and editing. **Hemin Zhang:** Conceptualization, Funding acquisition, Project administration, Supervision, Writing - original draft.

## Declaration of Competing Interest

The authors declare that they have no known competing financial interests or personal relationships that could have appeared to influence the work reported in this paper.

## Data availability

Data will be made available on request.

## Acknowledgments

This work was supported by the National Natural Science Foundation of China (No. 52276207), Sichuan Science and Technology Foundation (2022YFG0264), the Fundamental Research Funds for Central Universities (20826041G4185), and Climate Change Response Project (NRF-2019M1A2A2065612), Brainlink Project (NRF-2022H1D3A3A01081140), and Korea-China Key Joint Research Program (2017K2A9A2A11070341) funded by the Ministry of Science and ICT of Korea, and by the 2019 Research Fund (1.190013.01) of UNIST.

## Appendix A. Supporting information

Supplementary data associated with this article can be found in the online version at [doi:10.1016/j.apcatb.2023.123465](https://doi.org/10.1016/j.apcatb.2023.123465).

## References

- A. Fujishima, K. Honda, Electrochemical photolysis of water at a semiconductor electrode, *Nature* 238 (1972) 37, <https://doi.org/10.1038/238037a0>.
- M.P. Suryawanshi, U.V. Ghorpade, C.Y. Toe, U.P. Suryawanshi, M. He, D. Zhang, J. S. Jang, S.W. Shin, J.H. Kim, X. Hao, R. Amal, Earth-abundant photoelectrodes for water splitting and alternate oxidation reactions: recent advances and future perspectives, *Prog. Mater. Sci.* 134 (2023), 101073, <https://doi.org/10.1016/j.pmatsci.2023.101073>.
- T.H. Jeon, D. Monllor-Satoca, Gh Moon, W. Kim, Hi Kim, D.W. Bahnmann, H. Park, W. Choi, Ag(I) ions working as a hole-transfer mediator in photoelectrocatalytic water oxidation on  $\text{WO}_3$  film, *Nat. Commun.* 11 (2020) 967, <https://doi.org/10.1038/s41467-020-14775-2>.
- V. Andrei, G.M. Ucoski, C. Pommernroj, C. Uswachoke, Q. Wang, D.S. Achilleos, H. Kasap, K.P. Sokol, R.A. Jagt, H. Lu, T. Lawson, A. Wagner, S.D. Pike, D. S. Wright, R.L.Z. Hoye, J.L. MacManus-Driscoll, H.J. Joyce, R.H. Friend, E. Reisner, Floating perovskite- $\text{BiVO}_4$  devices for scalable solar fuel production, *Nature* 608 (2022) 518, <https://doi.org/10.1038/s41586-022-04978-6>.
- Y.H. Ng, A. Iwase, A. Kudo, R. Amal, Reducing graphene oxide on a visible-light  $\text{BiVO}_4$  photocatalyst for an enhanced photoelectrochemical water splitting, *J. Phys. Chem. Lett.* 1 (2010) 2607–2612, <https://doi.org/10.1021/jz100978u>.
- P. Wang, H. Wu, Y. Tang, R. Amal, Y.H. Ng, Electrodeposited  $\text{Cu}_2\text{O}$  as photoelectrodes with controllable conductivity type for solar energy conversion, *J. Phys. Chem. C* 119 (2015) 26275–26282, <https://doi.org/10.1021/acs.jpcc.5b07276>.
- H. Zhang, S.O. Park, S.H. Joo, J.H. Kim, S.K. Kwak, J.S. Lee, Precisely-controlled, a few layers of iron titanate inverse opal structure for enhanced photoelectrochemical water splitting, *Nano Energy* 62 (2019) 20, <https://doi.org/10.1016/j.nanoen.2019.05.025>.
- O. Zandi, T.W. Hamann, Determination of photoelectrochemical water oxidation intermediates on haematite electrode surfaces using operando infrared spectroscopy, *Nat. Chem.* 8 (2016) 778, <https://doi.org/10.1038/nchem.2557>.
- H. Zhang, D. Li, W.J. Byun, X. Wang, T.J. Shin, H.Y. Jeong, H. Han, C. Li, J.S. Lee, Gradient tantalum-doped hematite homojunction photoanode improves both photocurrents and turn-on voltage for solar water splitting, *Nat. Commun.* 11 (2020) 4622, <https://doi.org/10.1038/s41467-020-18484-8>.
- G.M. Carroll, D.K. Zhong, D.R. Gamelin, Mechanistic insights into solar water oxidation by cobalt-phosphate-modified  $\alpha\text{-Fe}_2\text{O}_3$  photoanodes, *Energy Environ. Sci.* 8 (2015) 577–584, <https://doi.org/10.1039/c4ee02869d>.
- U. Bjoerksten, J. Moser, M. Graetzel, Photoelectrochemical studies on nanocrystalline hematite films, *Chem. Mater.* 6 (1994) 858–863, <https://doi.org/10.1021/cm00042a026>.
- J.Y. Kim, G. Magesh, D.H. Youn, J.W. Jang, J. Kubota, K. Domen, J.S. Lee, Single-crystalline, wormlike hematite photoanodes for efficient solar water splitting, *Sci. Rep.* 3 (2013) 2681, <https://doi.org/10.1038/srep02681>.
- D.A. Wheeler, G. Wang, Y. Ling, Y. Li, J.Z. Zhang, Nanostructured hematite: synthesis, characterization, charge carrier dynamics, and photoelectrochemical properties, *Energy Environ. Sci.* 5 (2012) 6682, <https://doi.org/10.1039/c2ee00001f>.
- T.H. Jeon, G.-h Moon, H. Park, W. Choi, Ultra-efficient and durable photoelectrochemical water oxidation using elaborately designed hematite nanorod arrays, *Nano Energy* 39 (2017) 211–218, <https://doi.org/10.1016/j.nanoen.2017.06.049>.
- K.-Y. Yoon, J. Park, M. Jung, S.-G. Ji, H. Lee, J.H. Seo, M.-J. Kwak, S. Il Seok, J. H. Lee, J.-H. Jang,  $\text{NiFeO}_x$  decorated  $\text{Ge}$ -hematite/perovskite for an efficient water splitting system, *Nat. Commun.* 12 (2021) 4309, <https://doi.org/10.1038/s41467-021-24428-7>.
- Z. Zhang, T. Tsuchimochi, T. Ina, Y. Kumabe, S. Muto, K. Ohara, H. Yamada, S. L. Ten-no, T. Tachikawa, Binary dopant segregation enables hematite-based heterostructures for highly efficient solar  $\text{H}_2\text{O}_2$  synthesis, *Nat. Commun.* 13 (2022) 1499, <https://doi.org/10.1038/s41467-022-28944-y>.
- Z. Zhang, I. Karimata, H. Nagashima, S. Muto, K. Ohara, K. Sugimoto, T. Tachikawa, Interfacial oxygen vacancies yielding long-lived holes in hematite mesocrystal-based photoanodes, *Nat. Commun.* 10 (2019) 4832, <https://doi.org/10.1038/s41467-019-12581-z>.
- L.K. Dhandoor, T.S. Koh, P. Anushkaran, H.-S. Chung, W.-S. Chae, H.H. Lee, S. H. Choi, M. Cho, J. Suk Jang, Enhanced charge transfer with tuning surface state in hematite photoanode integrated by niobium and zirconium co-doping for efficient photoelectrochemical water splitting, *Appl. Catal. B Environ.* 315 (2022), 121538, <https://doi.org/10.1016/j.apcatb.2022.121538>.
- L. Kumar Dhandoor, P. Anushkaran, W.-S. Chae, H.-S. Chung, H.-H. Lee, S. Hee Choi, M. Cho, J. Suk Jang, Efficient charge transfers in hematite photoanode integrated by fluorine and zirconia co-doping for photoelectrochemical water splitting, *Chem. Eng. J.* 446 (2022), 136957, <https://doi.org/10.1016/j.cej.2022.136957>.
- G. Liu, S. Ye, P. Yan, F. Xiong, P. Fu, Z. Wang, Z. Chen, J. Shi, C. Li, Enabling an integrated tantalum nitride photoanode to approach the theoretical photocurrent limit for solar water splitting, *Energy Environ. Sci.* 9 (2016) 1327, <https://doi.org/10.1039/c5ee03802b>.
- J. Deng, Y. Li, Y. Xiao, K. Feng, C. Lu, K. Nie, X. Lv, H. Xu, J. Zhong, Improved water oxidation of  $\text{Fe}_2\text{O}_3/\text{Fe}_2\text{TiO}_5$  photoanode by functionalizing with a hydrophilic organic hole storage overlayer, *ACS Catal.* 12 (2022) 7833, <https://doi.org/10.1021/acscatal.22c01328>.
- K. Zhang, B. Jin, C. Park, Y. Cho, X. Song, X. Shi, S. Zhang, W. Kim, H. Zeng, J. H. Park, Black phosphorene as a hole extraction layer boosting solar water splitting of oxygen evolution catalysts, *Nat. Commun.* 10 (2019) 2001, <https://doi.org/10.1038/s41467-019-10034-1>.
- D.H. Seo, S.Y. Hong, T.H. You, A. Sivanantham, I.S. Cho, Using a  $\text{CeO}_2$  quantum dot hole extraction-layer for enhanced solar water splitting activity of  $\text{BiVO}_4$  photoanodes, *Chem. Eng. J.* 450 (2022), 137917, <https://doi.org/10.1016/j.cej.2022.137917>.
- J.-B. Pan, X. Liu, B.-H. Wang, Y.-A. Chen, H.-Y. Tan, J. Ouyang, W. Zhou, S. Shen, L. Chen, C.-T. Au, S.-F. Yin, Conductive MOFs coating on hematite photoanode for activity boost via surface state regulation, *Appl. Catal. B Environ.* 315 (2022), 121526, <https://doi.org/10.1016/j.apcatb.2022.121526>.
- J. Xiao, H. Huang, Q. Huang, X. Li, X. Hou, L. Zhao, R. Ma, H. Chen, Y. Li, Remarkable improvement of the turn-on characteristics of  $\alpha\text{-Fe}_2\text{O}_3$  photoanode for photoelectrochemical water splitting with coating a  $\text{FeCoW}$  oxy-hydroxide gel, *Appl. Catal. B Environ.* 212 (2017) 89, <https://doi.org/10.1016/j.apcatb.2017.04.075>.
- H. Zhang, J.H. Park, W.J. Byun, M.H. Song, J.S. Lee, Activating the surface and bulk of hematite photoanodes to improve solar water splitting, *Chem. Sci.* 10 (2019) 10436, <https://doi.org/10.1039/c9sc04110a>.
- H. Zhang, W.Y. Noh, F. Li, J.H. Kim, H.Y. Jeong, J.S. Lee, Three birds, one-stone strategy for hybrid microwave synthesis of Ta and Sn codoped  $\text{Fe}_2\text{O}_3@\text{FeTaO}_4$  nanorods for photo-electrochemical water oxidation, *Adv. Funct. Mater.* 29 (2019) 1805737, <https://doi.org/10.1002/adfm.201805737>.
- J.H. Kim, Y.J. Jang, S.H. Choi, B.J. Lee, J.H. Kim, Y.B. Park, C.-M. Nam, H.G. Kim, J.S. Lee, A multitude of modifications strategy of  $\text{ZnFe}_2\text{O}_4$  nanorod photoanodes for enhanced photoelectrochemical water splitting activity, *J. Mater. Chem. A* 6 (2018) 12693, <https://doi.org/10.1039/c8ta02161a>.
- H. Ma, W. Chen, Q. Fan, C. Ye, M. Zheng, J. Wang, Regulating Sn self-doping and boosting solar water splitting performance of hematite nanorod arrays grown on fluorine-doped tin oxide via low-level Hf doping, *J. Colloid Interface Sci.* 625 (2022) 585, <https://doi.org/10.1016/j.jcis.2022.06.055>.

[30] G.M. Morishita, I. Rodríguez-Gutiérrez, R.H.R. Castro, F.L. Souza, Hafnium boosts charge carrier dynamics in hematite for improved solar water splitting, *Mater. Lett.* 340 (2023), 134176, <https://doi.org/10.1016/j.matlet.2023.134176>.

[31] J.H. Kim, J.H. Kim, J.W. Jang, J.Y. Kim, S.H. Choi, G. Magesh, J. Lee, J.S. Lee, Awakening solar water-splitting activity of  $ZnFe_2O_4$  nanorods by hybrid microwave annealing, *Adv. Energy Mater.* 5 (2015) 1401933, <https://doi.org/10.1002/aenm.201401933>.

[32] L.M. Zheng, X.R. Wang, W.M. Lu, C.J. Li, T.R. Paudel, Z.Q. Liu, Z. Huang, S. W. Zeng, K. Han, Z.H. Chen, X.P. Qiu, M.S. Li, S. Yang, B. Yang, M.F. Chisholm, L. W. Martin, S.J. Pennycook, E.Y. Tsymbal, J.M.D. Coey, W.W. Cao, Ambipolar ferromagnetism by electrostatic doping of a manganite, *Nat. Commun.* 9 (2018) 1897, <https://doi.org/10.1038/s41467-018-04233-5>.

[33] Y. Liu, J. Zhang, Y. Li, Q. Qian, Z. Li, Y. Zhu, G. Zhang, Manipulating dehydrogenation kinetics through dual-doping  $Co_3N$  electrode enables highly efficient hydrazine oxidation assisting self-powered  $H_2$  production, *Nat. Commun.* 11 (2020) 1853, <https://doi.org/10.1038/s41467-020-15563-8>.

[34] H. Zhang, Y.K. Kim, H.Y. Jeong, J.S. Lee, A few atomic  $FeNbO_4$  overlayers on hematite nanorods: microwave-induced high temperature phase for efficient photoelectrochemical water splitting, *ACS Catal.* 9 (2019) 1289–1297, <https://doi.org/10.1021/acscatal.8b04034>.

[35] Y. Zhao, K.R. Yang, Z. Wang, X. Yan, S. Cao, Y. Ye, Q. Dong, X. Zhang, J.E. Thorne, L. Jin, K.L. Materna, A. Trimpalis, H. Bai, S.C. Fakra, X. Zhong, P. Wang, X. Pan, J. Guo, M. Flytzani-Stephanopoulos, G.W. Brudvig, V.S. Batista, D. Wang, Stable iridium dinuclear heterogeneous catalysts supported on metal-oxide substrate for solar water oxidation, *Proc. Natl. Acad. Sci. USA* 115 (2018) 2902, <https://doi.org/10.1073/pnas.1722137115>.

[36] A.Z. Khan, T.A. Kandiell, S. Abdel-Azeim, T.N. Jahangir, K. Alhooshani, Phosphate ions interfacial drift layer to improve the performance of CoFe-Prussian blue hematite photoanode toward water splitting, *Appl. Catal. B Environ.* 304 (2022), 121014, <https://doi.org/10.1016/j.apcatb.2021.121014>.

[37] S. Kmient, P. Schmuki, Z. Hubicka, L. Machala, R. Kirchgeorg, N. Liu, L. Wang, K. Lee, J. Olejnicek, M. Cada, I. Gregora, R. Zboril, Photoanodes with fully controllable texture: the enhanced water splitting efficiency of thin hematite films exhibiting solely (110) crystal orientation, *ACS Nano* 9 (2015) 7113, <https://doi.org/10.1021/acsnano.5b01740>.

[38] W. Liu, Y. Dong, J. Liu, L. Zhang, Y. Lu, H. Lin, Halloysite nanotube confined interface engineering enhanced catalytic oxidation of photo-Fenton reaction for aniline aerofloat degradation: Defective heterojunction for electron transfer regulation, *Chem. Eng. J.* 451 (2023), 138666, <https://doi.org/10.1016/j.cej.2022.138666>.

[39] A. Puthirath Balan, S. Radhakrishnan, C.F. Woellner, S.K. Sinha, L. Deng, C. L. Reyes, B.M. Rao, M. Paulose, R. Neupane, A. Apte, V. Kochat, R. Vajtai, A. R. Harutyunyan, C.W. Chu, G. Costin, D.S. Galvao, A.A. Marti, P.A. van Aken, O. K. Varghese, C.S. Tiwary, A. Malie Madom Ramaswamy Iyer, P.M. Ajayan, Exfoliation of a non-van der Waals material from iron ore hematite, *Nat. Nanotechnol.* 13 (2018) 602, <https://doi.org/10.1038/s41565-018-0134-y>.

[40] H. Zhang, P. Li, H. Zhou, J. Xu, Q. Jiang, J.H.L. Hadden, Y. Wang, M. Wang, S. Chen, F. Xie, D.J. Riley, Unravelling the synergy of oxygen vacancies and gold nanostars in hematite for the electrochemical and photoelectrochemical oxygen evolution reaction, *Nano Energy* 94 (2022), 106968, <https://doi.org/10.1016/j.nanoen.2022.106968>.

[41] C. Shao, A.S. Malik, J. Han, D. Li, M. Dupuis, X. Zong, C. Li, Oxygen vacancy engineering with flame heating approach towards enhanced photoelectrochemical water oxidation on  $WO_3$  photoanode, *Nano Energy* 77 (2020), 105190, <https://doi.org/10.1016/j.nanoen.2020.105190>.

[42] J. Xiao, F. Zhao, J. Zhong, Z. Huang, L. Fan, L. Peng, S.-F. Zhou, G. Zhan, Performance enhancement of hematite photoanode with oxygen defects for water splitting, *Chem. Eng. J.* 402 (2020), 126163, <https://doi.org/10.1016/j.cej.2020.126163>.

[43] R. Timm, A.R. Head, S. Yngman, J.V. Knutsson, M. Hjort, S.R. McKibbin, A. Troian, O. Persson, S. Urpelainen, J. Knudsen, J. Schnadt, A. Mikkelsen, Self-cleaning and surface chemical reactions during hafnium dioxide atomic layer deposition on indium arsenide, *Nat. Commun.* 9 (2018) 1412, <https://doi.org/10.1038/s41467-018-03855-z>.

[44] Y.R. Luo, *Comprehensive Handbook of Chemical Bond Energies*, CRC Press, Boca Raton, FL, 2007.

[45] Y. Han, J. Wu, Y. Li, X. Gu, T. He, Y. Zhao, H. Huang, Y. Liu, Z. Kang, Carbon dots enhance the interface electron transfer and photoelectrochemical kinetics in  $TiO_2$  photoanode, *Appl. Catal. B Environ.* 304 (2022), 120983, <https://doi.org/10.1016/j.apcatb.2021.120983>.

[46] P. Wang, D. Li, H. Chi, Y. Zhao, J. Wang, D. Li, S. Pang, P. Fu, J. Shi, C. Li, Unveiling the hydration structure of ferrilhydrite for hole storage in photoelectrochemical water oxidation, *Angew. Chem. Int. Ed.* 60 (2021) 6691–6698, <https://doi.org/10.1002/anie.202014871>.

[47] F. Le Formal, K. Sivula, M. Grätzel, The transient photocurrent and photovoltage behavior of a hematite photoanode under working conditions and the influence of surface treatments, *J. Phys. Chem. C* 116 (2012) 26707–26720, <https://doi.org/10.1021/jp308591k>.

[48] Y. Song, X. Zhang, Y. Zhang, P. Zhai, Z. Li, D. Jin, J. Cao, C. Wang, B. Zhang, J. Gao, L. Sun, J. Hou, Engineering  $MoO_x/MXene$  hole transfer layers for unexpected boosting of photoelectrochemical water oxidation, *Angew. Chem. Int. Ed.* 61 (2022), e202200946, <https://doi.org/10.1002/anie.202200946>.

[49] T. Jiao, C. Lu, D. Zhang, K. Feng, S. Wang, Z. Kang, J. Zhong, Bi-functional  $Fe_2ZrO_5$  modified hematite photoanode for efficient solar water splitting, *Appl. Catal. B Environ.* 269 (2020), 118768, <https://doi.org/10.1016/j.apcatb.2020.118768>.

[50] Y. Zhao, H. Xie, W. Shi, H. Wang, C. Shao, C. Li, Unravelling the essential difference between  $TiO_x$  and  $AlO_x$  interface layers on  $Ta_3N_5$  photoanode for photoelectrochemical water oxidation, *J. Mater. Chem. A* 64 (2022) 33–37, <https://doi.org/10.1016/j.jchem.2021.04.042>.

[51] Y. Zhao, G. Liu, H. Wang, Y. Gao, T. Yao, W. Shi, C. Li, Interface engineering with an  $AlO_x$  dielectric layer enabling an ultrastable  $Ta_3N_5$  photoanode for photoelectrochemical water oxidation, *J. Mater. Chem. A* 9 (2021) 11285–11290, <https://doi.org/10.1039/dta00206f>.

[52] Y. Li, Q. Mei, Z. Liu, X. Hu, Z. Zhou, J. Huang, B. Bai, H. Liu, F. Ding, Q. Wang, Fluorine-doped iron oxyhydroxide cocatalyst: promotion on the  $WO_3$  photoanode conducted photoelectrochemical water splitting, *Appl. Catal. B Environ.* 304 (2022), 120995, <https://doi.org/10.1016/j.apcatb.2021.120995>.

[53] Y. Sun, H. Li, Y. Hu, J. Wang, A. Li, P.F.-X. Corvini, Single-atomic ruthenium coupling with NiFe layered double hydroxide in-situ growth on  $BiVO_4$  photoanode for boosting photoelectrochemical water splitting, *Appl. Catal. B Environ.* 340 (2024), 123269, <https://doi.org/10.1016/j.apcatb.2023.123269>.

[54] P. Wang, P. Fu, J. Ma, Y. Gao, Z. Li, H. Wang, F. Fan, J. Shi, C. Li, Ultrathin cobalt oxide interlayer facilitated hole storage for sustained water oxidation over composited tantalum nitride photoanodes, *ACS Catal.* 11 (2021) 12736, <https://doi.org/10.1021/acscatal.1c03298>.

[55] O. Zandi, T.W. Hamann, Enhanced water splitting efficiency through selective surface state removal, *J. Phys. Chem. Lett.* 5 (2014) 1522–1526, <https://doi.org/10.1021/jz500535a>.

[56] A. Tsyanok, P. Monroy-Castillero, Y. Pieckner, A. Yochelis, A. Rothschild, Parallel water photo-oxidation reaction pathways in hematite photoanodes: implications for solar fuel production, *Energy Environ. Sci.* 15 (2022) 2445, <https://doi.org/10.1039/d1ee03953a>.

[57] A. Tsyanok, P. Monroy-Castillero, Y. Pieckner, A. Yochelis, A. Rothschild, Parallel water photo-oxidation reaction pathways in hematite photoanodes: implications for solar fuel production, *Energy Environ. Sci.* 15 (2022) 2445–2459, <https://doi.org/10.1039/D1EE03953A>.

[58] T.H. Jeon, C. Park, U. Kang, G.-h Moon, W. Kim, H. Park, W. Choi, Photoelectrochemical water oxidation using hematite modified with metal-incorporated graphitic carbon nitride film as a surface passivation and hole transfer overlayer, *Appl. Catal. B Environ.* 340 (2024), 123167, <https://doi.org/10.1016/j.apcatb.2023.123167>.

[59] J. Mo, Y. Ko, Y.S. Yun, J. Huh, J. Cho, A carbonization/interfacial assembly-driven electroplating approach for water-splitting textile electrodes with remarkably low overpotentials and high operational stability, *Energy Environ. Sci.* 15 (2022) 3815, <https://doi.org/10.1039/d2ee01510b>.